Single-well seismic imaging using the full waveform of an acoustic sonic

Louis Chabot, David C. Henley, R. James Brown and John C. Bancroft

ABSTRACT

The reservoir characteristics around the borehole play an important role in determining the success or the failure of a well. However the knowledge of such reservoir characteristics is not always complete. This work seeks to fill that gap by attempting to image scattered energy beyond the borehole wall. The imaging of that scattered energy is to be achieved by single-well seismic imaging using the full waveform acquired with a standard sonic well-logging tool. In the first part of this paper, a synthetic acoustic full-waveform sonic dataset is created on which a proposed processing flow is applied. The proposed processing flow successfully imaged a scatter point. In the second part of this paper another processing flow is proposed this time to image scattered energy beyond the borehole wall using real full-waveform field data. The image obtained shows promising indications of some dipping features, which are expected because of the inclination of the borehole with respect to the geological formations. However, the weakness of the reflections could be explained by a number of things, such as incompletely cancelled noise modes. Further work is thus required to improve on the two proposed processing flows.

INTRODUCTION TO SINGLE-WELL SEISMIC IMAGING

The motivation

Current borehole imaging logs, acquired either with an acoustic or a resistivity well-logging tool, normally look only at the surface of the borehole wall. Borehole imaging logs can provide valuable information to aid in reservoir description, such as fracture identification and stratigraphic interpretation.

However, there are at times ambiguous interpretations with current borehole imaging logs. For example, is the observed fracture set open or closed? If it is open, how far does it extend into the formation? Where is the top of the reservoir when drilling horizontally? Ambiguous interpretations can lead to expensive decisions such as perforating the wrong fracture set or steering the drill bit in the wrong direction.

Is single-well seismic imaging the answer?

Definitions

Today, there are several varieties of borehole seismic imaging: tomography or cross-well imaging (transmitter in one borehole and receiver in another), vertical seismic profiling (transmitter on the surface and receiver in a borehole), and single-well seismic imaging (transmitter and receiver in the same borehole). Single-well seismic imaging is practised in different ways. There is single-well imaging using a borehole seismic source with clamped receivers in the same borehole: for example, to image the flank of a salt dome; and there is single-well imaging using a well-logging

tool: for example, to evaluate the elastic properties of geologic formations. The focus of this work is on single-well seismic imaging using a well-logging tool.

Previous work

As an example of work done on single-well seismic imaging, Hornby (1989) used an experimental acoustic well-logging tool equipped with one monopole source and 12 receivers, each recording 20ms of full-waveform data, to compute an image of structural changes beyond the borehole wall. With the source and receiver array both passing through the structures that cross the borehole, downdip and updip structures could be imaged separately (Figure 1).
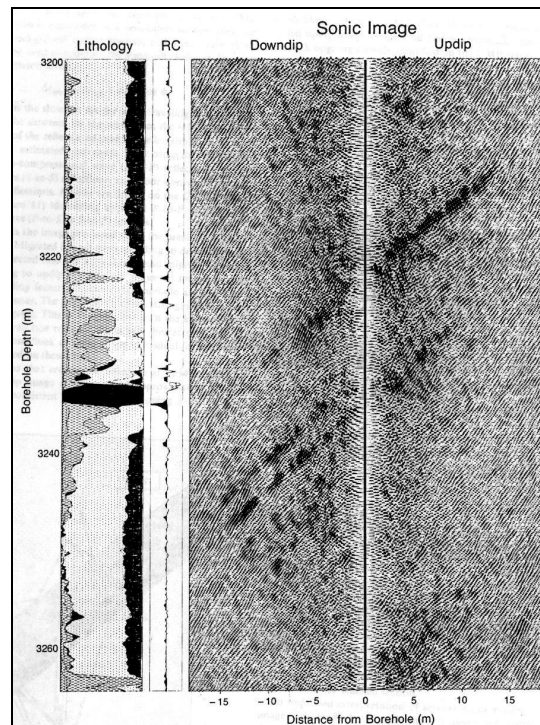

FIG. 1. Sonic image displayed against a lithology analysis and a P-wave reflectivity estimate. The angle of dip of the strongest feature in the migrated image corresponds to the known angle of the borehole with respect to the bedding. The sonic image represents a section of the borehole 60 m in length (Hornby, 1989).

In his single-well imaging effort, Hornby (1989) removed the direct P waves, P and S headwaves, as well as the Stoneley arrivals from the records using an *f-k* filter. Then, he applied a back-projection operator to the prestack velocity-filtered sonic data, followed by a common midpoint stack (6-fold). Finally, he migrated the data with a generalized Radon transform to image the scatter energy.

Since the time of Hornby's (1989) work, acoustic well-logging technologies have much evolved. Now well-logging tools are not only built with longer spacing, enabling them to look deeper into the formation, but also are equipped with electronics that provide them with better ability to record the full waveform. Also, better signal-processing technologies enable the successful identification of not only

compressional, but also shear and Stoneley arrivals. Coates et al. (2000) took advantage of those advances and generated imaging results for a horizontal well. However the method of processing the full waveform was not described.

Objectives

The objective of this work is thus to investigate the acoustic and elastic wave propagation in and around an open borehole with the purpose of creating a processing-imaging flow applicable to a full-waveform sonic data to image scattered energy from beyond the borehole walls.

SOME PRINCIPLES OF WAVE PROPAGATION IN AND AROUND THE BOREHOLE

The acoustic-wave propagation in a fluid-filled borehole is constrained differently than the acoustic-wave propagation in the more classic marine seismic reflection survey. The geometric properties of the fluid-filled borehole allow for both partial and complete trapping of wave energy, greatly enhancing the amplitude of acoustic signals detected at positions along the borehole axis (Paillet and Cheng, 1991). Also the source in the borehole normally operates in the kilohertz frequency range.

The theory of acoustic-wave propagation in a fluid-filled borehole has been covered in textbooks (e.g. Paillet and Cheng, 1991). In general, for a fast formation, "an omnidirectional pressure source radiates a compressional wave pulse out into the borehole fluid, which propagates into the surrounding formation. As this pulse enters the formation, it excites both compressional and shear waves in the formation" (Schlumberger, 1997). As the compressional and shear waves propagate in the formation, they generate head waves in the borehole fluid (at critical incidence angle) and thus produce refracted arrivals. As those same compressional and shear waves propagate in the formation, they are likely to encounter acoustic-impedance contrasts. Those acoustic-impedance contrasts scatter energy back towards the borehole where the receivers of the well-logging tool are located. After the head waves, the more complicated interface waves such as the Stoneley waves arrive (Figure 2).

The first arrivals have historically been the primary subject of interest. For a source-receivers array located on the borehole axis of a borehole of uniform radius r_1, Equation (1) provides key relations to calculate the different traveltimes associated with the arrivals of the P wave. In Equation (1), t_d is the traveltime of the direct arrival, t_r that of the reflected arrival and t_h that of the head-wave arrival for a given source-receiver offset x recorded over a sequence of two homogeneous concentric layers one being the fluid of velocity v_1 with a given thickness r_1 and the other being the borehole wall material of velocity v_2. The critical angle of incidence is defined as θ_c.

$$t_d = \frac{x}{v_1}; \quad t_r^2 = t_0^2 + \frac{x^2}{v_1^2}; \quad t_h = \frac{x}{v_2} + t_1, \quad t_1 = \frac{2 \times r_1 \times \cos(\theta_c)}{v_1}, \quad \sin(\theta_c) = \frac{v_1}{v_2}. \quad (1)$$
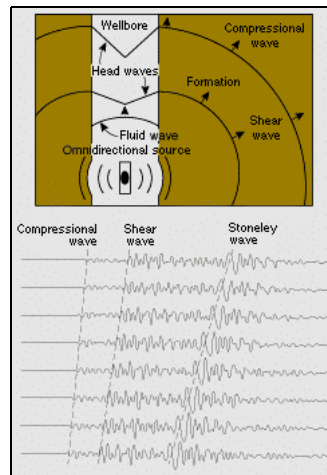
FIG. 2. Illustrates in cross-section the theoretical acoustic and elastic wave propagation in the borehole fluid and around the borehole. This is applicable for fast formation where the shear velocity is higher than the acoustic velocity of the fluid. The corresponding theoretical recorded wavetrain at the well-logging tool for eight different offsets along the borehole axis is also shown in this diagram. Note the theoretical recorded wavetrain could also contain scattered energy from beyond the borehole walls (after Schlumberger, 1997).

For body waves, since S waves cannot propagate in a fluid, an incident P wave, upon striking a liquid-solid interface, generates a reflected P wave and a transmitted P and S waves. At a liquid-solid interface the normal displacement, μ_z, and the normal stress, σ_{zz}, must be continuous across the boundary. On the other hand, the tangential stress, σ_{xz}, in the solid must be zero at the interface while the tangential displacement, μ_x, need not be continuous because the liquid can slide across the interface. These boundary conditions govern the Zoeppritz equations regulating the reflection and transmission coefficients for an incident P-wave. The direct and head waves have the tendency to obscure the shallow reflections at large offsets (Figure 3).

Each of the interface waves displays a specific behaviour. The tube-wave is a coupled wave mode intrinsically involving both the fluid and the borehole wall expanding and contracting as the pressure wave passes. Most tube-wave travels axially, their amplitudes decreasing slowly with distance as they travel along the borehole axis. Stoneley and pseudo-Rayleigh waves propagate along the borehole wall and die away exponentially into the formation surrounding the borehole. In particular, the Stoneley waves are, in general, slightly dispersive with both group and phase velocities close to 0.9 times the P wave fluid velocity. Stoneley waves are present at all frequencies. On the other hand, the pseudo-Rayleigh waves cannot exist below a minimum frequency where their velocity equals the S wave velocity in the surrounding rock (Sheriff and Gelhart, 1995). At higher frequencies (greater than 30 kHz) the velocity of both Stoneley and pseudo-Rayleigh waves approach the P wave fluid velocity. In general, the interface waves constitute an important source of coherent noise and obscure the deeper reflections at smaller offsets (Figure 3).
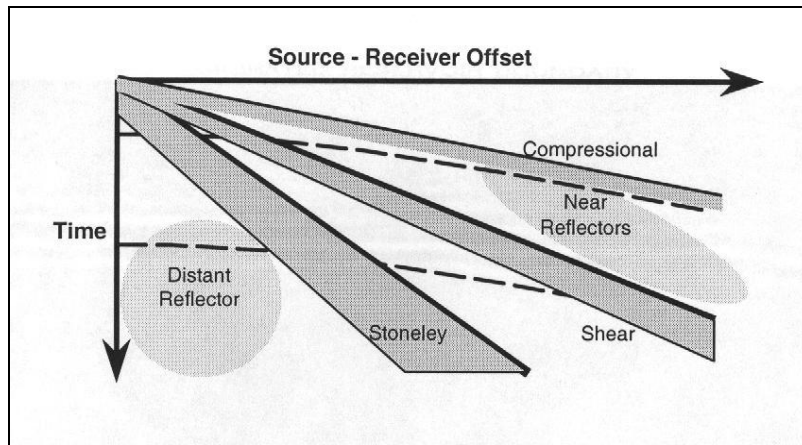
FIG. 3. The two shaded areas represent the quiet zones where the scattered signal may be seen (Coates et al., 2000).

In addition, the waveform appearance is influenced by the following parameters: the source-receiver spacing, the rock properties of the borehole wall, and the frequency of the source, which can excite different modes depending on the cut-off frequencies and attenuation, Q^{-1} (Paillet and Cheng, 1991). The diameter of the borehole also plays an important role in controlling the different propagating modes. Those parameters will have a combined impact on the observed full waveform.

As the compressional and shear waves propagate in the formation, they may encounter acoustic-impedance contrasts. These contrasts scatter energy back towards the borehole where the receivers of the well-logging tool are located. In the recorded waveform there is thus also the possibility of recording energy arrivals originating away from the borehole walls. This is the energy that we are interested in.

WAVEFORM PROCESSING AND IMAGING OF SINGLE-WELL SEISMIC SYNTHETIC DATA

Creation of a full waveform synthetic dataset

To yield insight into the propagation of waves from a monopole source in a fluid-filled borehole, it became necessary to carry out numerical modelling of acoustic-wave propagation in a fluid-filled borehole. There exist finite-difference programs applicable to the modelling of acoustic-wave propagation in a borehole (for example, Wu et al., 2001) but none were available to us. As an alternative, for this particular application, a two-dimensional finite-difference modelling code was selected where the formulation is fourth-order in space and second-order in time. The finite-difference code was provided by G.T. Schuster, J. Xu and Y. Luo (University of Utah) and is based on an algorithm described by Levander (1988). Additional modifications to the code were made by Guevara (2001). The advantages of the staggered-grid scheme of this algorithm lie in its stability and accuracy for modelling materials with large Poisson's ratio and mixed acoustic-elastic media (Levander, 1988).

It is important to recognize that although a two-dimensional model does not adequately model the cylindrical geometry of the borehole environment, the fluid layer analogy of the two-dimensional model gives a qualitative approximation to the physical mechanism of mode trapping and constructive interference that characterizes waveform logs (Paillet and Cheng, 1991).

The model presented here is two-dimensional, characterized by a horizontal fluid layer confined above and below by identical elastic layers with the top layer having a scatter point embedded into it. The horizontal fluid layer simulates the fluid-filled borehole. A scale factor of 1:333 (real:modelled) was used to replicate the borehole environment in its main features. As seen in Figure 4, the model dimensions are 3000m in length by 1000m in depth. The borehole has a diameter of 200m. The borehole layer is filled with a fluid that has a P-velocity of 1500m/s and a density of 1000kg/m^3. The media located immediately on either side of the borehole fluid have a P-velocity of 2600m/s and a density of 1700kg/m^3. Finally, the scatterer is of dimension 20m by 20m, has a P-velocity of 3600m/s and a density of 5000kg/m^3. It is important to note that scatterpoints of different dimensions were tested before choosing a scatterpoint of dimensions of 20m by 20m. Those trials were conducted in order to ensure that the scatterpoint would be small enough to behave as a true scatterpoint but large enough to be captured by the simulation grid. The advantage of this model is that reflectors can be formed from the superposition of appropriately positioned scatterpoints.
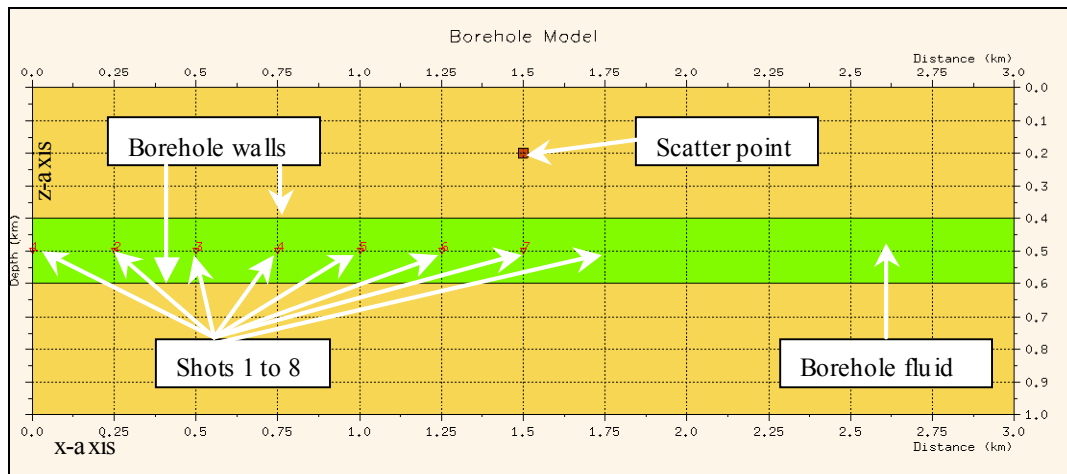

FIG. 4. Diagram showing the borehole model with one scatterpoint. The distance axis is defined as the *x*-axis while the depth axis is defined as the *z*-axis. Note the presence of the scatterpoint located at (1500, 200). There are eight shot points, spaced 250 m apart along the borehole axis, in the fluid-filled borehole.

Although an "explosive" source would have been the preferred method of generating the compressive force of the well-logging source, the source models available with the numerical model limited us. Of the two source models available (line source and plane wave), the one that was the most suited for our application was the *x*-component line-source particle-velocity model, a line source with the polarization in the *x*-direction (i.e. in the direction of the borehole axis). The wavelet

selected for this line source was a zero-phase 30Hz Ricker wavelet having duration of 130ms (time signal). Although the Ricker wavelet is not closely related to the known response of piezoelectric sources (Tsang and Rader, 1979), it has been used extensively in the seismic literature to represent impulse sources and its mathematical properties are well known. The line source was located in the fluid-filled borehole at a point on the borehole axis.

A series of receivers were placed along the borehole axis to record the particle velocity (both the *x*- and the *z*- components of particle velocity). A receiver spacing of 10m was used. The listening time at each receiver was 1600ms. Note that the well-logging tool is not accounted for in the borehole and thus the receivers lie suspended in the fluid-filled borehole.

In building the finite-difference model, care was taken to respect the minimum wavelength, λ_{min}, and the stability criterion, *S*, as described in Equation (2). In this equation, Δx, refers to the selected space step in both the horizontal and vertical directions (note that $\Delta z = \Delta x$), Δt, refers to the selected time step while v_{min} and v_{max} represents the minimum and the maximum velocity of the model.

$$\lambda_{min} = \frac{v_{min}}{f_{min} \times 2.5} > \Delta x \times 5; \quad S = v_{max} \times \frac{\Delta t}{\Delta x} < 0.606 \tag{2}$$

The wavefield generated by the finite-difference modelling calculation was saved in a series of snapshots at different times. These were plotted with the help of Matlab™. Figure 5 shows a sample snapshot of the wavefield at 400ms. Note that it took normally 10 hours to generate each shot record.

The snapshot in Figure 5 displays the wavefield in the borehole fluid and in the surrounding formation at a time of 400ms in two formats. The top portion shows the horizontal component (*x*-direction) of the wavefield while the bottom portion shows the vertical component (*z*-direction) of the same wavefield. In this snapshot, the vertical axis is the *z*-direction and represents the depth in metres in the borehole model, while the horizontal axis is the *x*-direction and represents the distance along the borehole axis in metres. Undisturbed borehole fluid and formation are represented as uniform grey. Components of particle velocity in the borehole fluid and formation are represented on a grey scale from white (negative) to black (positive).

Again in reference to Figure 5, the generation of the direct P and the P head wave in the fluid can be observed. Behind the head wave in the borehole are the interface waves such as the Stoneley wave. The guided borehole waves are generated from the source pulse in the borehole fluid, which is reflected from the formation many times. With each reflection, compressional waves are excited in the formation. Also, one can observe the evanescent nature of the Stoneley wave, which travels along the borehole wall more slowly than the fluid wave.
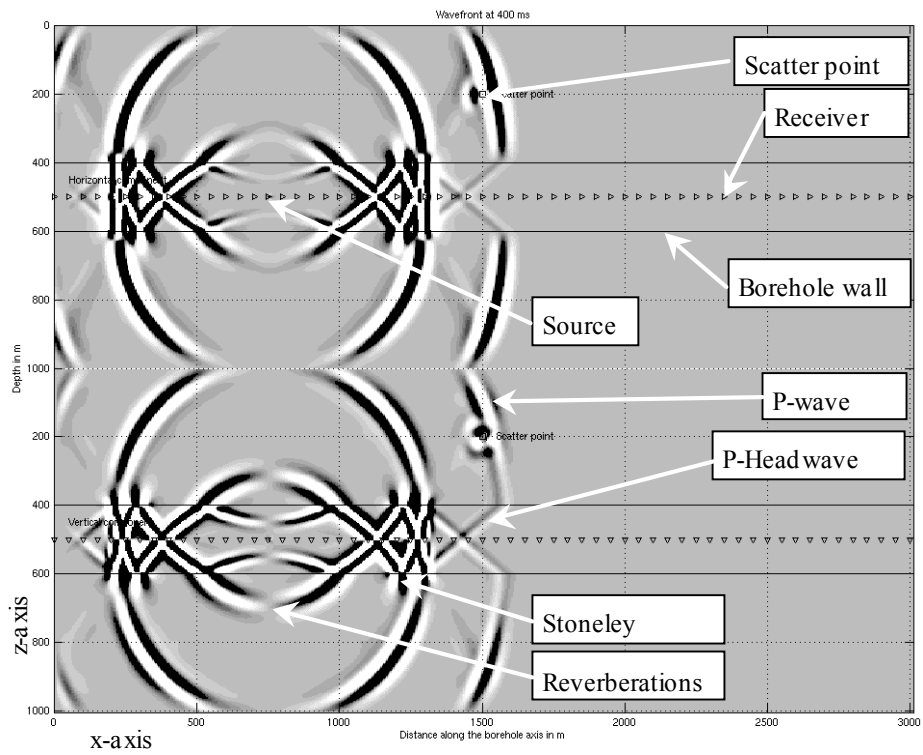
FIG. 5. Snapshot of the wavefield at 400ms. The source, polarized in the *x*-direction, was located in the fluid-filled borehole on the borehole axis at a distance of 750 m.
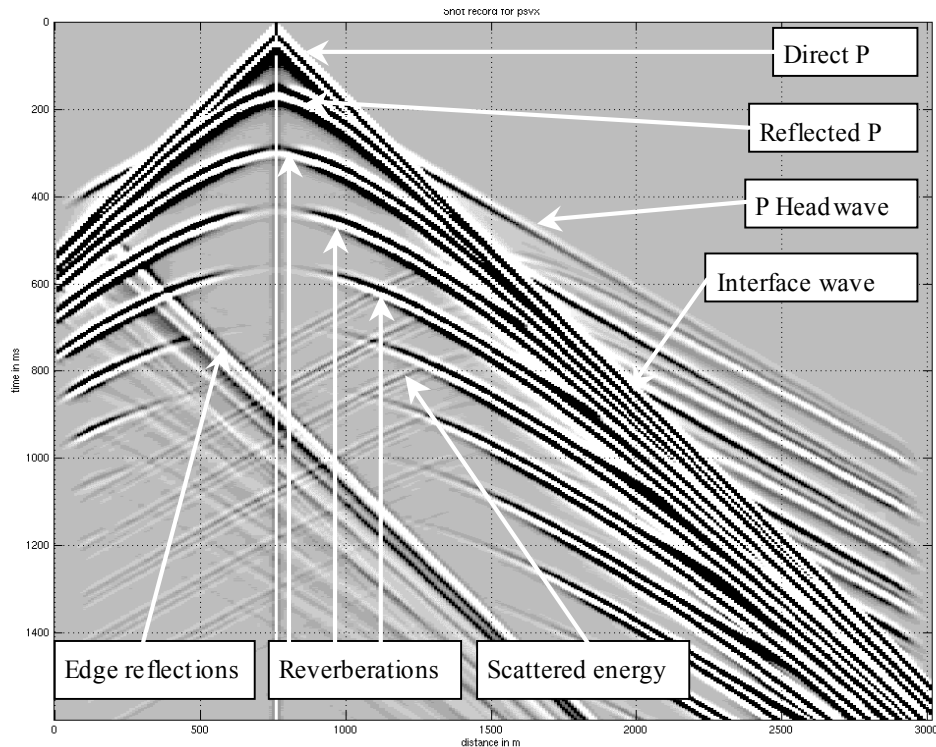
FIG. 6. Raw shot record recorded by 300 receivers located along the borehole axis.

Figure 6 illustrates a shot record of the horizontal component of particle velocity measured at the receivers along the borehole axis. This shot record represent a first approximation of the pressure field that would be recorded by borehole hydrophones. Note the complexity of the shot record. The following can be observed: the direct P wave (at 1500m/s), the P reflection from the borehole wall (at $t_0 = 133$ms), the P headwave (at 2600m/s), and the interface-wave arrivals such as the Stoneley. Note also the strong presence of reverberations (at $t_0 = 266$ms, 400ms, 533ms, 667ms and at 800ms) in the shot record. Also note the reflections from the edge of the model appearing on the left-hand side of the shot record. More importantly, notice the presence of the scattered energy in the shot record. This is our target signal for imaging.

The shot record obtained from this numerical simulation can be compared to actual waveform data acquired in the field (Figure 11). When comparing the two we noticed the absence of strong reverberations in the field data. This difference between the simulated and the field data full-waveform could be accounted for by the difference between the 2-D geometry of the model and the 3-D geometry of the real world.

To conduct the imaging experiment, a total of five shots records (numbered 1, 4, 6, 7 and 8 in Figure 4) at a nominal spacing of 250m were acquired along the borehole axis. The outputs were exported to ProMAX™ where the waveform processing and imaging flow were tested.

Proposed processing flow for the synthetic dataset

In processing the synthetic results, the first step consisted in assigning the appropriate geometry to the borehole environment. As a result, the *x*-coordinates along the borehole axis were relabeled from the original ascending order from left to right (Figure 4) to a descending order from left to right (Figure 7) creating negative offset below the shot coordinate and positive offset above the shot coordinate.

To recover the scattered energy present in the shot records, the interface waves and the reflections from the edge of the model were filtered-out by subtracting the shot record generated without the scatter point present (homogeneous case) from the original shot record that contained the effect of the scatter point (non-homogeneous case). Although this filtering technique cannot be applied to real data, it is an approach that will ensure that we identify all the scattered energy. Therefore, this filtering technique was applied to all five simulated shots records, to produce the filtered synthetic acoustic dataset, an example of which can be seen in Figure 7.

The focusing and imaging of the filtered synthetic data were next achieved with the use of the equivalent-offset migration (EOM). As a first step to EOM, common-scatter-point (CSP) gathers were formed using a binning size of 5m with a migration aperture of a maximum of 1250m. The selection of the migration aperture is important because it is the spatial envelope of traces that will contribute in focusing the scattered energy. The result of the application of this first step of EOM to the synthetic dataset is presented in Figure 8 in a one-sided CSP gather format.
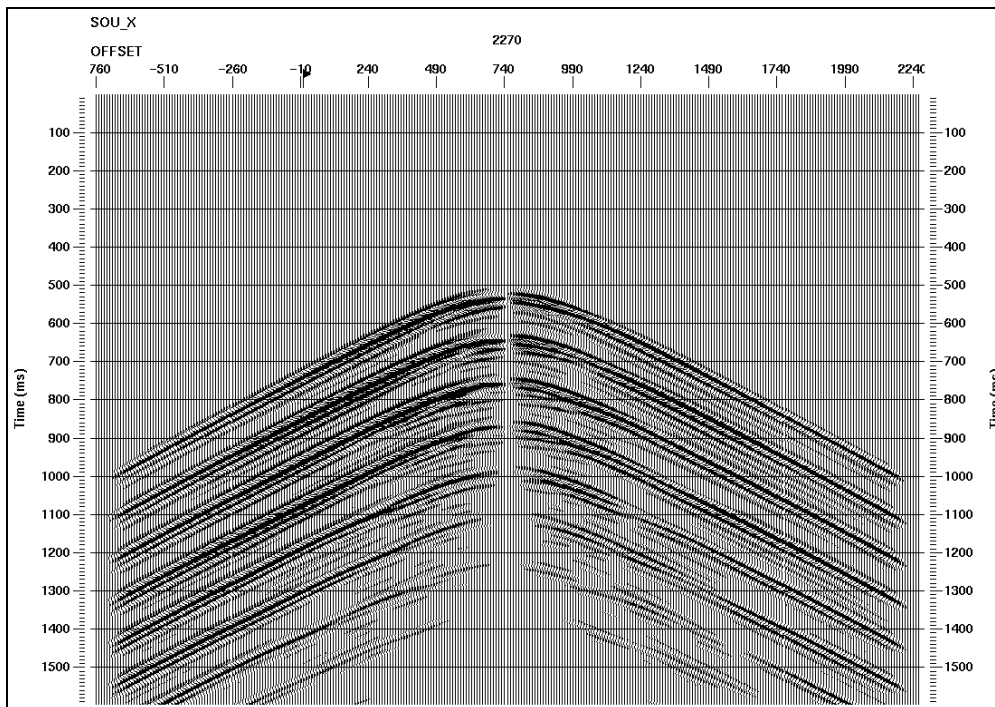

FIG. 7. Difference shot record acquired along the borehole axis. Note the presence in this shot record of only the P scattered energy (at 2600m/s). The reverberations in the borehole generate the observed multiples.
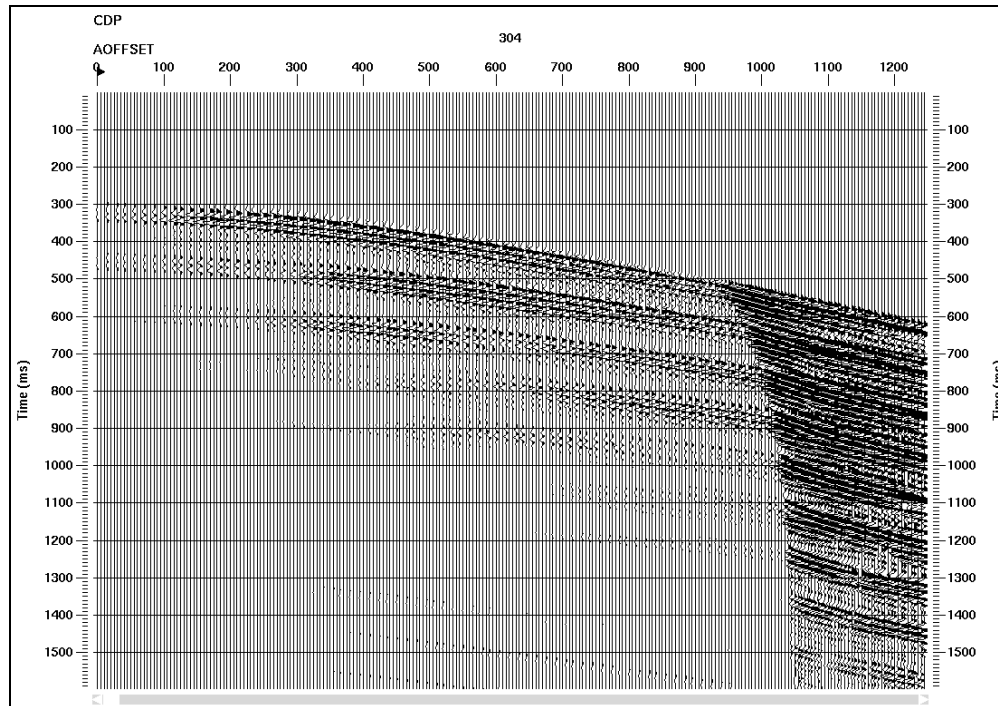
FIG. 8. One-sided CSP gather of the synthetic acoustic data at CSP location 304. This CSP location corresponds to a CSP panel located immediately below the scatterpoint.

Equivalent-offset migration (EOM) is a prestack time migration made up of several steps (Bancroft et al., 1998). The first step consists of forming prestack migration gathers from the input traces called common-scatter-point (CSP) gathers. The CSP gathers are generated by mapping input traces to an equivalent offset h_e. This step is followed by a focusing process that applies a simplified Kirchhoff migration to the CSP gathers, involving scaling, filtering and normal-moveout (NMO) correction. The final step consists in stacking the "corrected" gathers. The objective of this prestack time migration is to collect all the scattered energy and relocate it to the position of the scatterpoint.

The EOM was selected as the preferred method of imaging in this work because a CSP gather has a higher fold and a larger offset range than a common-midpoint (CMP) gather and is more likely to contain coherent scattered energy from scattering point. In particular, the maximum equivalent offset of the CSP gather is equal to the migration aperture and is much larger than the maximum source-receiver offset of the CMP gathers. Also, EOM has been successfully used not only to image regular seismic data but also to image vertical-array data (Bancroft and Xu, 1999).

A scatterpoint impulse response in the prestack volume (*x, h, t*) yield a traveltime surface called a Cheop's pyramid. Equation (3) is the reformulation of the double-square-root equation and provides the relations needed to map the traces from the seismogram, one to one, in a CSP gather. In Equation (3), h_e is the equivalent offset, h_{cmp} is the distance from the CMP location of the input trace to the CSP, *h* is the half

source-receiver offset, T_t is the recorded time and T_α, is the first useful sample in time of a trace on the CMP to be mapped to a fixed offset bin in the CSP gather. In general a CSP gather taken at the scatter point location will yield a hyperbola.

$$h_e^2 = h_{cmp}^2 + h^2 - \left(\frac{2 \times h_{cmp} \times h}{T_t \times v_{mig}}\right)^2 \; ; \quad T_\alpha = \frac{2 \times h_{cmp}}{v_{rms}} \; ; \quad v_{mig} = v_{rms} = \sqrt{\frac{t_1 \times v_1^2 + t_2 \times v_2^2}{T_t}} \; . (3)$$

Once the CSP gathers were formed, the next step in the EOM method consisted in applying NMO correction to the individual CSP gathers. The velocity model selected for the proper application of the NMO to the synthetic dataset corresponded to the calculated RMS velocity of the model using Equation (3). Once this step was completed, a straight stack was applied to the NMO-corrected data to generate the final image in time. The result is presented in Figure 9.
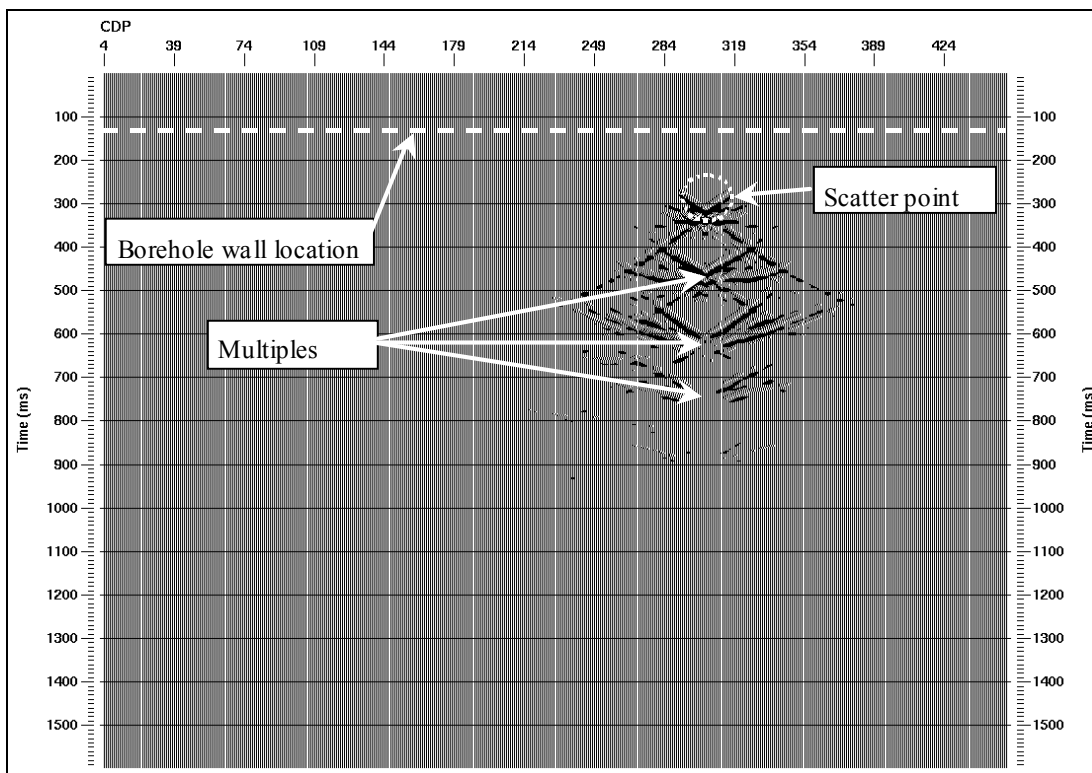

FIG. 9. With the help of the proposed processing flow, the energy from the scatterpoint is focused at approximately CSP 304 and 310 ms (white dashed circle). This location closely corresponds to the expected position of the scatter point at CSP 304 and 287 ms. Note that, because of the multiple energy created by the reverberations, predominantly between the borehole wall and the scatterpoint, there are several ghosts of the scatterpoint present later in time (440ms, 595ms and 750ms).

WAVEFORM PROCESSING AND IMAGING OF SINGLE-WELL SEISMIC FIELD DATA

The full-waveform field dataset

A full-waveform sonic field dataset was acquired in the 8-8-23-23W4 well, located in the Blackfoot field in Alberta. This dataset consists of 310m of full-waveform data, which was acquired in the section of the well that intersected, at about 20° from the vertical, a thick flat-lying sequence of alternating sandstones and shales. The data were acquired with the Schlumberger dipole shear sonic imager or DSI™ well-logging tool (Figure 10) in a monopole configuration, at a centre frequency of 12kHz. Receivers were located 15cm apart on the tool with a near-offset distance to the source of 2.74m. Eight full waveforms were recorded simultaneously at the firing of the monopole source. Each waveform was recorded with a sample interval of 10μs for a total of 512 samples/waveform (Harrison et al., 1990).
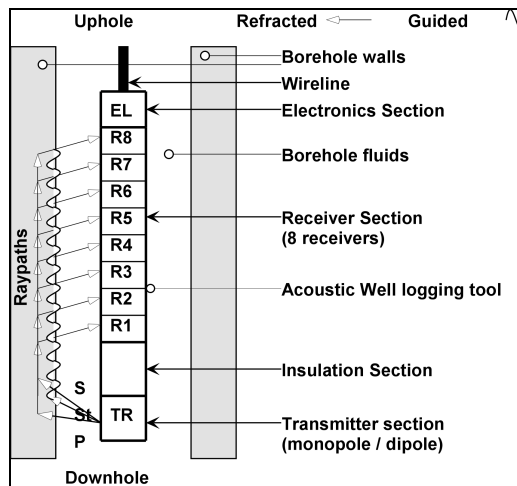

FIG. 10. The acoustic well-logging tool DSI™ used to acquire the full-waveform dataset (modified after Schlumberger, 1997).

Figure 11 illustrates eight full waveforms simultaneously recorded in a single firing of the monopole source of the DSI™ well-logging tool. This sample of 8 full waveforms was taken at source depth of 1422.73m from the 8-8-23-23W4 well. An initial look reveals the presence in the full waveform of coherent energy with linear moveouts: the compressional (3810m/s), shear (2177m/s) and Stoneley (1226m/s) arrivals. These waveforms could also contain energy scattered from beyond the borehole wall.
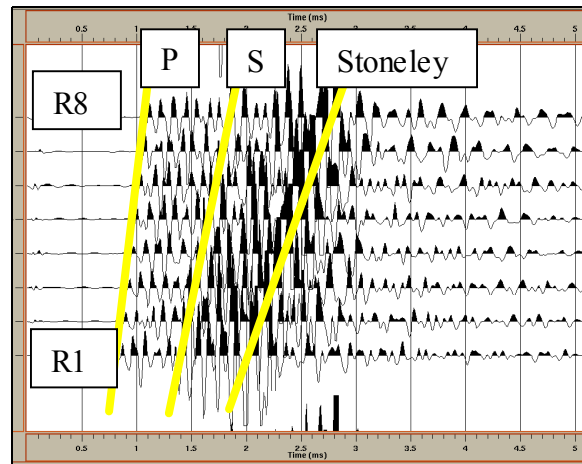
FIG. 11. Identification of P, S and Stoneley arrivals in the acquired full waveform. The horizontal scale is in ms.

Figure 12 displays three CMP gathers of 8 traces each from this dataset. Although 4 traces would be expected in the CMP, these CMP gathers presented here attempt to present more information by using a bin size (0.15m) twice as large as the standard bin size (0.075m).
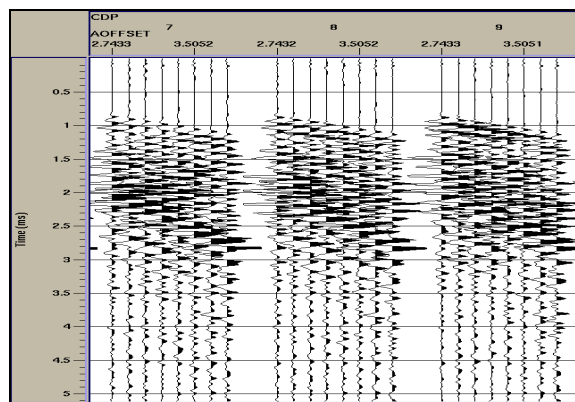

FIG. 12. Example of contiguous common-midpoint (CMP) records. CMP records are made up of 8 traces each.

Proposed processing flow for the field dataset

To image energy that has been scattered from beyond the borehole wall, several processing steps were needed. The processing of the full-waveform data in this work was completed with ProMAX™ seismic processing software.

Before processing the data, we first assigned geometry appropriate to the borehole environment. Next, radial-trace filtering (Henley, 1999) was applied to the shot records to attenuate the strong linear arrivals of the shear and of the Stoneley waves. The Stoneley arrivals are especially bothersome in the shot records since they are characterized by high amplitudes and low frequencies and are present on all traces. The advantage of the radial trace filtering is that it is able to focus on localized events rather than widespread family of events (e.g. *f-k*). Next the filtered shot gathers were

trace-balanced since the amplitudes of the traces at 2.5ms and later times are much smaller than the amplitudes of the traces at 2.5ms and earlier times (see Figure 11). This step was next followed by the EOM.

For the CSP mapping, a velocity of 4000m/s was chosen from the average P velocity recorded by the well log over the zone of interest. Also a migration aperture of 20m, corresponding to a velocity of 4000m/s for a 5.12ms record, was selected after several trials. The migration aperture is very important since it is the spatial envelope of traces that will contribute scattered energy. It is important to note that the CSP gathers can be generated either with absolute equivalent-offset (one-sided), as seen in the previous section, or with signed, positive and negative, equivalent-offset (two-sided). Figure 13 shows a two-sided CSP gather. Linear, diffracted and dipping energies can be more completely observed on the two-sided CSP gather than on the one-sided CSP gather. As a result, the two-sided gather was selected for further processing.
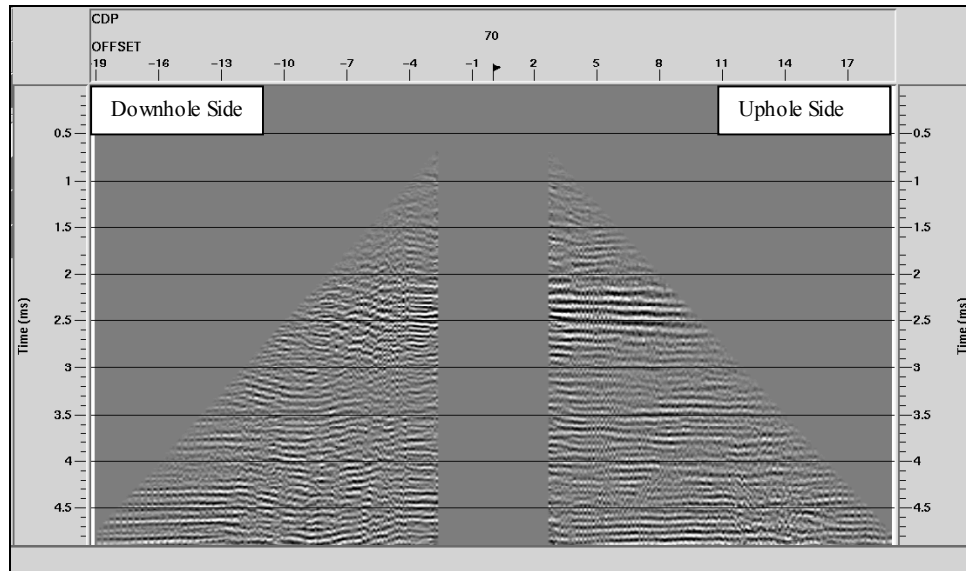
FIG. 13. Sample two-sided CSP gather located at CSP 70 (approximate location of the Viking sandstone). A total of 340 traces are included in this CSP gather. The negative offsets represent the dowhole side of the CSP while the positive offsets represent the uphole side of the CSP. Equivalent-offset dimension is in metres.
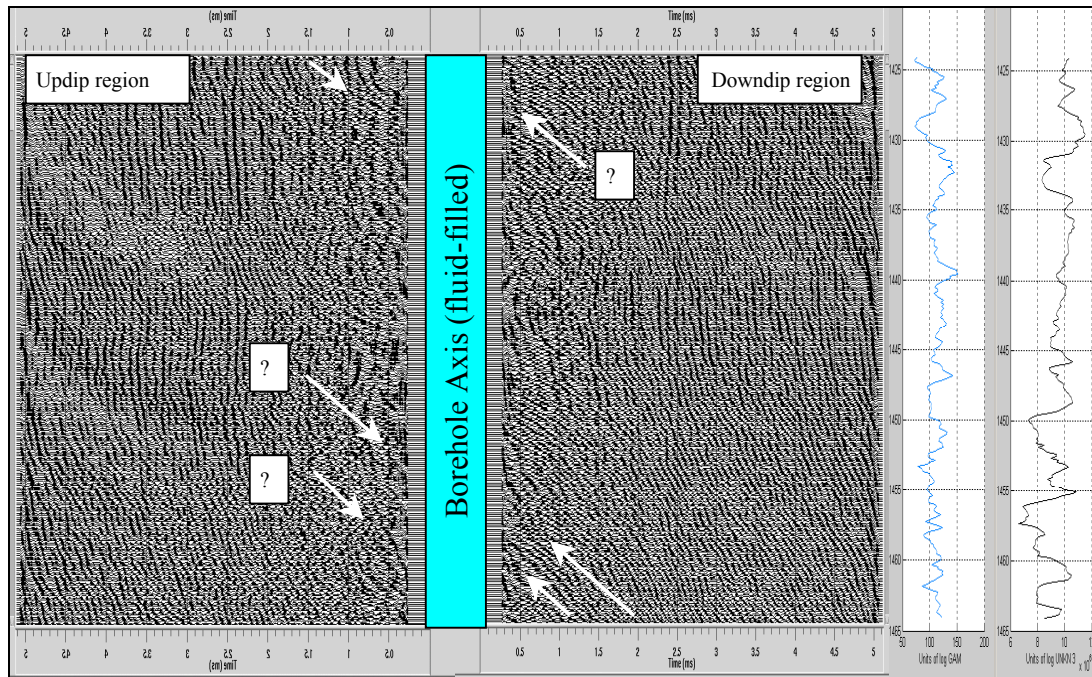
FIG. 14. Prestack time-migration image of the full-waveform data. The sonic image represents a cross-section view of apparent features intersecting the borehole. The borehole section is 40m in measured length. The lateral extent of investigation, away from either side of the borehole wall, is 5.12ms. To the left of the sonic image is displayed the corresponding natural gamma-ray log (lithology), scaled from 50 to 200 API units, and an acoustic impedance log, scaled from 6 to 12 x 10^6 m/s kg/m^3.

Once the CSP gathers were constructed, a constant-velocity analysis was run on the CSP gathers in order to define a "velocity model". This model was used later to apply NMO to the CSP gathers. At this stage, the two-sided CSP gathers were split into two separate families of gathers. The CSP gathers with negative offsets, looking downhole, were sorted together representing the updip portion of the borehole, while those with positive offsets, looking uphole, were sorted together representing the downdip portion of the borehole. Once this separation was completed, the CSP gathers representing the updip portion of the hole had NMO with the correct velocities applied to it, followed by a conventional CDP stack, thus creating the prestack time migration image of the updip region of the hole. The family of CSP gathers representing the downdip portion of the hole also had NMO with the correct velocities applied to it, followed by a conventional CDP stack, thus creating the prestack time migration image of the downdip region of the hole. The results are presented in a composite image in Figure 14.

DISCUSSION

The proposed processing flow for the synthetic acoustic full-waveform sonic dataset was made up of two essential steps: the proper assignment of the geometry for the borehole environment and the application of EOM. In this flow the EOM consists of the following: the creation of one-sided CSP gathers, NMO, and straight stack.

Using the proposed processing flow for the synthetic dataset, the scatterpoint energy was successfully focused (Figure 9).

The proposed processing flow for the full-waveform sonic field dataset was made up of four essential steps: the proper assignment of the geometry for the borehole environment, the application of radial trace filtering to remove energy with linear moveout, trace balancing and the application of EOM. In this flow the EOM is comprised of the following: two-sided CSP gather, CSP gather sorted in updip and downdip, NMO and straight stack on the updip and downdip gathers separately.

Using the proposed processing flow for the field dataset the, prestack time migration result (Figure 14) looks promising. This image shows indication of some dipping features, which are expected because of the inclination of the borehole with respect to the geological formations. However the weakness of the reflections could be explained by a number of things, including weak reflecting boundaries, incompletely cancelled noise modes and the large angle (approximately 70°) made between the borehole and the geological units. In any case, this processing flow holds promise for application to real field data.

The borehole is a complex environment. It is important to bear in mind that the information from single-well seismic imaging needs to be used in conjunction with other well-log data.

FUTURE WORK

This research work is currently in progress, with the following items for future work.

First, we are currently searching for an axial-geometry finite-difference modelling program in order to generate more accurate synthetic results on which to train the proposed processing flows.

Second, additional processes for the processing of the synthetic full-waveform data need to be explored, such as (not necessarily in order): deconvolution, dereverberation with predictive deconvolution, geometrical spreading and Q^{-1}, application of statics using first arrivals, application of statics using borehole caliper logs (e.g. for borehole washouts), and the definition of a migration datum when the borehole is deviated and curved.

Third, we are in the process of locating the full-waveform sonic data that was acquired and processed in 1989 by Hornby, in order to test the proposed processing flow. Is the proposed processing flow improving the image?

Finally we are currently searching for a complete field dataset to test the mature processing method on. The complete field dataset would have been acquired over a section of a borehole that makes a small angle with the geological beds that it intersects. This complete field dataset would include not only the full-waveform sonic acquired over the zone of interest but also include directional (dip and azimuth),

lithological (gamma ray, density, etc.) and imaging data (looking at the surface of the borehole wall) over the zone of interest.

ACKNOWLEDGEMENTS

REFERENCES

Bancroft, J.C., Geiger, H.D., and Margrave, G.F., 1998, The equivalent offset method of prestack time migration: Geophysics, **63**, 2042 - 2053.

Bancroft, J.C. and Xu, Y., 1999, Equivalent offset migration for vertical receiver arrays, SEG, Expanded Abstracts, 1374-1377.

Coates, R., Kane, M., Chang, C., Esmersoy, C., Fukuhara, M., and Yamamoto, H., 2000, Single-well sonic imaging: High-definition reservoir cross-sections from horizontal wells, SPE 65457.

Guevara, S.E., 2001, Analysis and filtering of near-surface effects in land multicomponent seismic data, M.Sc. thesis, University of Calgary.

Harrison, A.R., Randall, C.J., Aron, J.B., Morris, C.F., Wignall, A.H., Dworak, R.A., Rutledge, L.L., and Perkins, J.L., 1990, Acquisition and analysis of sonic waveforms from a borehole monopole and dipole source for the determination of compressional and shear speeds and their relation to rock mechanical properties and surface seismic data: SPE 20557.

Henley, D.C., 1999, The radial trace transform: an effective domain for coherent noise attenuation and wavefield separation, 69th Annual International Meeting., SEG, Expanded Abstracts, 1204-1207.

Hornby, B.E., 1989, Imaging of near-borehole structure using full-waveform sonic data: Geophysics, **54**, 747-757.

Levander, A.R., 1988, Fourth-order finite-difference P-SV seismograms: Geophysics, **53**, 1425-1436.

Paillet, F.L. and Cheng, C.H., 1991, Acoustic waves in borehole: CRC Press.

Schlumberger, 1997, DSI™ – Dipole Shear Sonic Imager: Corporate brochure SMP-9200, 36 pages.

Sheriff, R.E. and Geldart, L.P., 1995, Exploration Seismology: Cambridge University Press.

Tsang, L. and Rader, D., 1979, Numerical evaluation of the transient acoustic waveform due to a point source in a fluid-filled borehole: Geophysics, **44**, 1706-1720.

Wu, C., Harris, J.M., and Franklin, J., 2001, Single-well seismic modeling in viscoelastic media using a variable grid finite difference method, 71st Annual International Meeting, SEG, Expanded Abstracts.